*High Power Laser Science and Engineering*, (2026), Vol. 14, e95, 9 pages.
doi:10.1017/hpl.2026.10178

HIGH POWER LASER SCIENCE AND ENGINEERING

RESEARCH ARTICLE

# Efficient tunable μJ-level 5.6–11 μm mid-infrared generation at 40 kHz via Raman-shifted multi-pass cell-driven difference-frequency generation

Junchang Su[1], Xincai Diao[3], Yang Liu[3], Junzhan Chen[2], Guorong Wu[3], and Wei Liu[2]

[1]*School of Physics and Astronomy, Sun Yat-sen University, Zhuhai, China*

[2]*School of Science, Sun Yat-sen University, Shenzhen, China*

[3]*Institute of Advanced Light Source Facilities, Shenzhen, China*

*(Received 11 May 2026 UTC; revised 8 June 2026 UTC; accepted 29 June 2026 UTC)*

**Abstract**

Efficient generation of microjoule-level long-wave mid-infrared pulses at high repetition rates remains challenging because conventional difference-frequency generation (DFG) systems typically rely on white-light-seeded optical parametric amplification (OPA) chains with limited overall efficiency. Here we demonstrate a Raman-shifted multi-pass-cell-driven DFG scheme for tunable 5.6–11 μm mid-infrared generation. A He–$CO_2$ molecular-gas multi-pass cell (MPC) efficiently converts 1025 nm pump pulses into a 1.10–1.25 μm signal through Raman-dominated red shifting, with a filtered-signal conversion efficiency of 17%–32% at repetition rates up to 40 kHz. The generated signal is combined with a synchronized 1025 nm pump beam and converted in a $LiGaS_2$ crystal. The system delivers 179 mW at 6 μm, corresponding to 4.5 μJ pulses and a pump-to-idler efficiency of 6.4%, and 168 mW at 7 μm with a maximum quantum efficiency of 41%. By replacing the OPA-based signal-generation chain with an efficient Raman-shifted molecular-gas MPC, this architecture offers a scalable route toward high-repetition-rate, high-energy long-wave mid-infrared ultrafast sources.

**Keywords:** difference-frequency generation; mid-infrared lasers; Raman-shifted multi-pass cell

## 1. Introduction

Ultrafast laser sources in the 5.6–11 μm spectral region are of strong interest because this band overlaps the molecular fingerprint window and many intense vibrational resonances in gases and condensed-phase materials[1–3]. Femtosecond sources in this wavelength range therefore enable chemically selective spectroscopy and imaging, strong-field light–matter interaction and resonant laser processing or surgery with enhanced material selectivity[4–7]. Recent demonstrations of selective mid-infrared femtosecond ablation of vascular tissues and dental enamel have further highlighted the practical value of high-performance long-wave mid-infrared sources for biomedical applications[8,9].

Ultrafast mid-infrared pulses in this spectral region are commonly generated by optical parametric amplification (OPA)[10–12], difference-frequency generation (DFG)[13–15] or intrapulse DFG (iDFG) driven by broadband few-cycle pulses[16,17]. Among these routes, DFG is particularly attractive for high-average-power operation, and the generated idler can be passively carrier-envelope-phase (CEP) stable when the pump and signal are derived from the same front-end laser[18,19]. The rapid development of Yb-based ultrafast lasers has made 1 μm sources especially appealing for this purpose, as they simultaneously provide high average power, high pulse energy and robust industrial-level operation. In parallel, non-oxide nonlinear crystals such as $LiGaS_2$ (LGS) have enabled 1-μm-pumped DFG deep into the long-wave mid-infrared region owing to their broad infrared transparency, relatively wide bandgap and high damage tolerance[20].

Despite these advantages, the signal-generation stage remains a central bottleneck in most 1-μm-pumped long-wave mid-infrared DFG systems. In conventional architectures, the signal wave is usually produced through white-light generation followed by one or multiple OPA stages before the final DFG crystal. Although this approach is versatile, it introduces substantial energy loss, alignment

Correspondence to: W. Liu, School of Science, Sun Yat-sen University, Shenzhen 518107, China. Email: liuwei95@mail.sysu.edu.cn

© The Author(s), 2026. Published by Cambridge University Press in association with Chinese Laser Press. This is an Open Access article, distributed under the terms of the Creative Commons Attribution licence (https://creativecommons.org/licenses/by/4.0), which permits unrestricted re-use, distribution and reproduction, provided the original article is properly cited.



Downloaded from https://www.cambridge.org/core. 18 Nov 2026 at 09:51:23, subject to the Cambridge Core terms of use.

complexity and additional sources of instability. For example, a representative 1-μm-pumped LGS-based 9 μm optical parametric chirped pulse amplification (OPCPA) system delivered 14 μJ pulses at 10 kHz, but the pump-to-mid-infrared efficiency was only approximately 0.9%[21]. In the undepleted DFG regime, the idler field scales with both the pump and signal fields; consequently, improving the efficiency and energy of the signal wave provides a direct route to higher idler efficiency while reducing the pump loading on the nonlinear crystal. This is beneficial for mitigating thermal effects and lowering the risk of optical damage.

The need for a more efficient signal arm is closely related to a broader performance gap in current long-wave mid-infrared ultrafast sources. Watt-level average powers have been achieved at high repetition rates, including multi-watt tunable systems in the 4–12 μm range operating from hundreds of kilohertz to megahertz[8,22]. Conversely, high pulse energies are more commonly obtained at low repetition rates, typically from 10 Hz to 1 kHz, with sub-mJ 9 μm pulses recently reported at 1 kHz[13]. Sources that simultaneously combine high-repetition-rate, microjoule-level pulse energy and efficient conversion in the 5.6–11 μm region remain comparatively rare. Overcoming the signal-generation bottleneck is therefore an important step toward bridging high-average-power and high-peak-field operating regimes.

Gas-filled multi-pass cells (MPCs) provide a promising platform for this purpose. MPCs have enabled nonlinear post-compression of ultrafast pulses to the kilowatt average-power and more than 100 mJ pulse-energy level, establishing them as one of the most scalable architectures in ultrafast nonlinear optics[23–25]. Few-cycle pulses produced by MPC compression have also been used for iDFG, generating tunable 4.5–9.5 μm radiation with tens of milliwatts of output power and efficiencies around 0.16%[26]. However, in iDFG the pump and signal portions are different spectral components of the same broadband pulse; their energy ratio, temporal duration and chirp cannot be optimized independently. An alternative strategy is to use an MPC not merely for few-cycle compression but also as a high-efficiency wavelength shifter that directly generates an energetic long-wavelength signal for a separate DFG stage. This architecture remains largely unexplored for high-repetition-rate long-wave mid-infrared generation.

Molecular gases are particularly suitable for nonlinear frequency shifting in MPCs owing to the coexistence of instantaneous electronic Kerr and delayed Raman nonlinearities. In contrast to noble gases, where nonlinear broadening is dominated by the instantaneous Kerr effect, molecular rotational excitation can enhance red-shifted spectral broadening and modify the spatiotemporal nonlinear dynamics[27]. Air-filled MPCs have recently become useful testbeds owing to their simplicity, and pure $N_2$ or $N_2O$ has also been investigated for enhanced spectral broadening and frequency shifting in MPC platforms[28–31]. Gases with strong rotational Raman nonlinearity are especially attractive for maximizing the long-wavelength shift and the usable signal energy. From this perspective, $CO_2$ offers a favorable balance of nonlinear response, availability and safe handling. In contrast, despite its strong delayed Raman response, the practical use of $N_2O$ is more restricted due to its neurotoxicity[32,33].

Here we demonstrate an efficient and scalable 5.6–11 μm ultrafast mid-infrared source based on Raman-shifted signal generation in a molecular-gas MPC followed by DFG in LGS. The key element is a He–$CO_2$-filled MPC that converts 1025 nm Yb-laser pulses into a tunable 1.10–1.25 μm signal with 17%–32% filtered-signal conversion efficiency at repetition rates up to 40 kHz. Helium is introduced as a buffer gas to suppress repetition-rate-dependent thermal degradation while preserving the Raman-enhanced spectral shift. The generated signal is then combined with a synchronized pump beam and converted in a 5.6-mm-thick LGS crystal. The system delivers 179 mW at 6 μm and 168 mW at 7 μm, corresponding to 4.5 and 4.2 μJ pulse energies, respectively. The maximum energy conversion efficiency reaches 6.4%, and the quantum efficiency reaches 41%. By replacing the conventional OPA-based signal arm with a Raman-shifted molecular-gas MPC, this work establishes a compact route toward efficient, high-repetition-rate, microjoule-level long-wave mid-infrared ultrafast sources.

## 2. Experimental setup

The experimental setup is shown in Figure 1. Both the pump and signal arms are derived from an Yb-laser source operating at 1025 nm, with a pulse duration of 200 fs, pulse energy up to 1 mJ and a repetition rate tunable from 1 to 120 kHz. The system is divided into three functional modules: Raman-shifted signal generation in a $CO_2$-based MPC, pump-arm delay control in a He-filled MPC and final DFG in an LGS crystal.

For Raman-induced signal generation, the 1025 nm pulses are coupled into a $CO_2$-filled MPC. Silver-enhanced mirrors with a reflectivity of approximately 99% are used to provide low dispersion over a broad spectral range. The cavity has a mirror radius of curvature of $R = 300$ mm and a length of $L = 580$ mm, supporting 33 passes and a total propagation length of approximately 19 m. Mode matching is performed with mirrors of focal lengths $f = -750$, 250, $-750$ and 2000 mm, yielding a beam waist of $w_0 = 165$ μm and a $1/e^2$ beam radius of $w_m = 730$ μm on the cavity mirrors. The beam waist is intentionally enlarged to increase the Rayleigh length and reduce local intensity, thereby mitigating ionization and thermal accumulation in the molecular gas. The MPC output is collimated to a beam diameter of 4.2 mm using a 1 m focal-length lens. Tunable signal pulses in the 1.10–1.25 μm range are obtained by filtering the Raman-induced red-shifted sidebands with long-pass filters

Downloaded from https://www.cambridge.org/core. 18 Nov 2026 at 09:51:23, subject to the Cambridge Core terms of use.

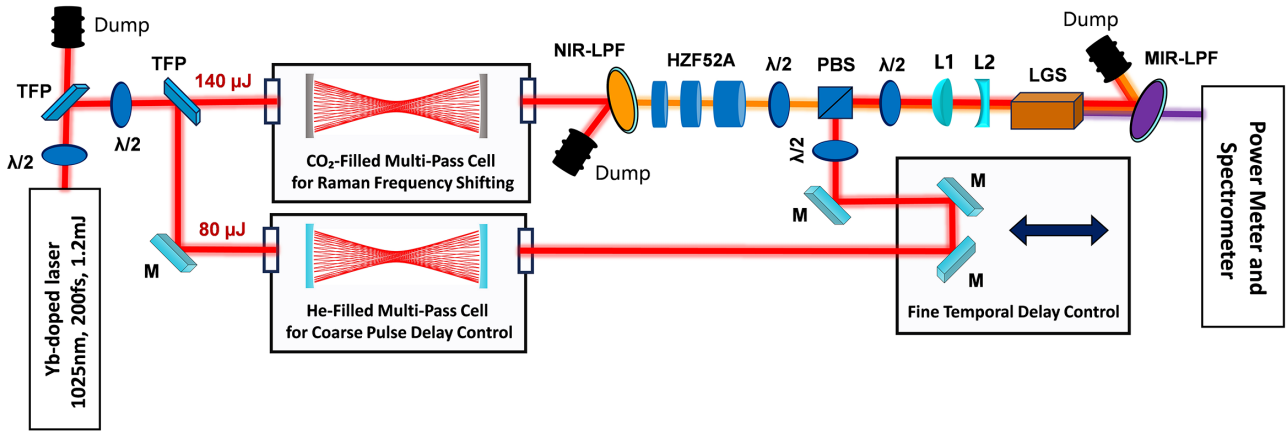



**Figure 1.** Experimental setup of the Raman-shifted MPC-driven mid-infrared DFG. TFP, thin-film polarizer; λ/2, half-wave plate; LPF, long-pass filter; L, lens; PBS, polarizing beam splitter; M, mirror.

having cut-on wavelengths of 1150, 1200 and 1250 nm. To improve temporal overlap with the 200 fs pump during DFG and to reduce the signal peak intensity in the nonlinear crystal, HZF52A glass plates with thicknesses of 1, 2 and 3 cm are inserted to positively chirp the signal pulses to approximately 300 fs.

A second MPC filled with He is placed in the pump arm. Its primary function is to provide a compact coarse optical delay that matches the propagation time of the Raman-shifted signal arm, while introducing a negligible nonlinear phase. This delay-line MPC has $R = 200$ mm, $L = 392$ mm and 46 passes, corresponding to a propagation length of approximately 18 m. Dielectric mirrors with reflectivity exceeding 99.9% provide a transmission efficiency of 96%. The cavity is filled with 0.5 bar He; the small nonlinear refractive index of He ($n_2 = 0.34 \times 10^{-24}\,\mathrm{m^2/(W \cdot atm)}$) suppresses nonlinear broadening while improving thermal conduction[34]. A set of lenses with focal lengths of 600, −150 and 400 mm is used for mode matching, yielding a beam waist of $w_0 = 92$ μm. The beam exiting the MPC is collimated to 4.2 mm using a mirror group with focal lengths of $f = -900$, −1000 and 900 mm. Fine temporal adjustment between the pump and signal pulses is achieved using a pair of vertically mounted mirrors on a translation stage.

The pump and signal beams are spatially combined using a half-inch polarizing beam splitter (PBS). A half-wave plate placed before the PBS controls the relative pump and signal energies, whereas another half-wave plate after the PBS sets the polarization for type-I phase matching in LGS. The combined beam is reduced to a diameter of approximately 1.8 mm using a telescope with focal lengths of $f = 0.35$ m and −0.15 m, and is then focused into a 5.6-mm-thick LGS crystal. The crystal features a 5.5 mm × 5.5 mm aperture and is anti-reflection coated. The generated mid-infrared radiation is separated using a 4.5 μm long-pass filter and characterized by power and spectral diagnostics.

Near-infrared spectra are measured using a Yokogawa AQ6370 optical spectrum analyzer, and mid-infrared spectra are measured using an FTIRZZ spectrometer. Near-infrared pulse durations are characterized with an APE pulseCheck autocorrelator. Beam pointing and beam quality are measured using WinCamD-LCM and WinCamD-IR-BB cameras for the near- and mid-infrared beams, respectively. Power and energy measurements are performed using a PHORAS 10 W power meter for the near-infrared beams and a Thorlabs S401C detector for the mid-infrared output.

## 3. Results

### *3.1. Raman-induced spectral evolution in a $CO_2$-filled MPC at 1 kHz*

Compared with noble gases, molecular gases possess additional rotational degrees of freedom that introduce a delayed nonlinear index change $\Delta n_\mathrm{d}$ in addition to the instantaneous electronic Kerr contribution $\Delta n_\mathrm{i}$. The accumulated nonlinear phase can therefore be written as follows:

$$\Delta\phi_\mathrm{NL} = \frac{2\pi L}{\lambda}(\Delta n_\mathrm{i} + \Delta n_\mathrm{d}),$$

where $L$ is the effective propagation length. A strong delayed Raman contribution increases the effective nonlinearity and, more importantly, drives an asymmetric frequency shift toward long wavelengths. This property is directly useful for generating the 1.10–1.25 μm signal required for efficient 1-μm-pumped long-wave mid-infrared DFG.

Figure 2 shows the output spectra of the 2 bar $CO_2$-filled MPC at 1 kHz as the input pulse energy is increased from 0 to 260 μJ. A pronounced Raman-dominated spectral evolution is observed, with strong asymmetry, a clear red shift and substantial enhancement of the long-wavelength sidebands. At an input energy of 260 μJ, the 20 dB bandwidth reaches 769 nm, corresponding to spectral coverage beyond one octave. To the best of our knowledge, this represents a record spectral bandwidth achieved from a 1 μm-driven

Downloaded from https://www.cambridge.org/core. 18 Nov 2026 at 09:51:23, subject to the Cambridge Core terms of use.

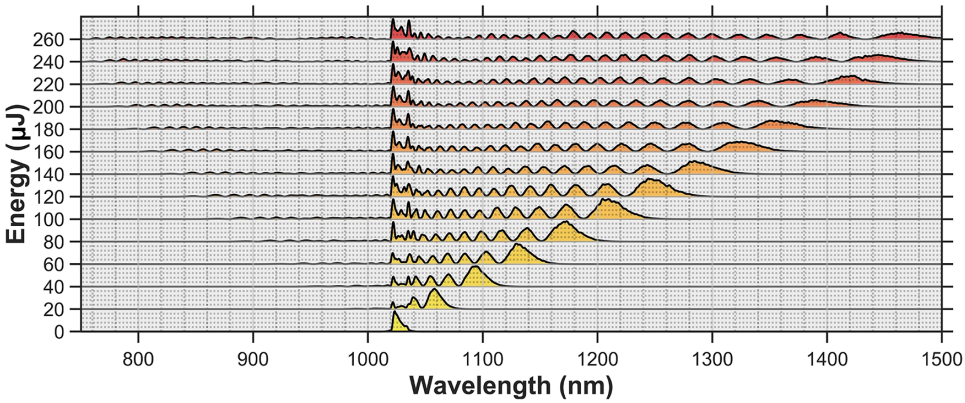



**Figure 2.** Evolution of the output spectrum from a 2 bar $CO_2$-filled MPC as a function of input pulse energy. The increasingly asymmetric red-shifted broadening indicates Raman-dominated nonlinear dynamics.

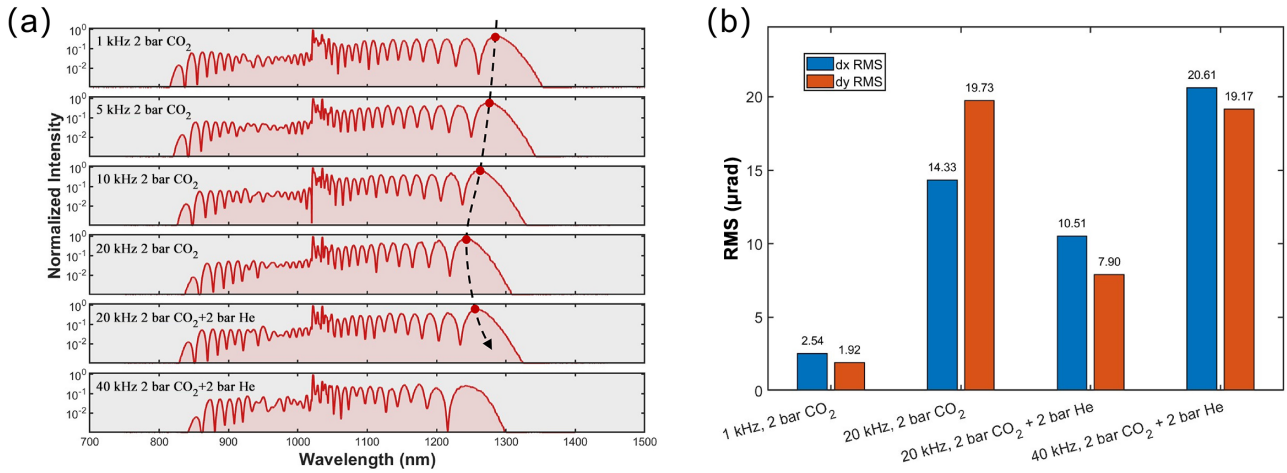



**Figure 3.** Repetition-rate scaling of the Raman-shifted MPC. (a) Spectral evolution in pure $CO_2$ and in a He–$CO_2$ mixture. (b) Beam pointing RMS fluctuations of the $CO_2$-based signal MPC.

MPC[35]. More importantly for the present work, a large fraction of the broadened spectrum is shifted into the 1.1–1.3 μm region, providing an efficient signal reservoir for subsequent DFG.

### *3.2. Repetition-rate scaling in a He–$CO_2$-filled MPC*

Under femtosecond excitation at elevated repetition rates, molecular gases with strong delayed Raman responses can suffer from thermal accumulation. As the average deposited heat increases, thermal effects weaken the rotational coherence and reduce the delayed nonlinear response. Figure 3(a) shows the spectral evolution of the pure $CO_2$-filled MPC as the repetition rate is increased from 1 to 20 kHz at a fixed input energy of 140 μJ and a pressure of 2 bar. The spectral broadening decreases monotonically with repetition rate: the 20 dB bandwidth decreases from approximately 513 nm at 1 kHz to 431 nm at 20 kHz. In contrast to hollow-core fibers, the transmission efficiency remains nearly constant at approximately 68% over this repetition-rate range, indicating the robustness of the MPC geometry against mode fluctuations and pointing perturbations[36,37].

To mitigate thermal degradation and extend the repetition rate, He is introduced as a buffer gas. The purpose of the He is not to provide additional nonlinearity, but rather to enhance thermal transport and accelerate collisional cooling while preserving the $CO_2$ Raman contribution[38]. Due to the safety pressure limit of the MPC (< 4 bar), we use a 1:1 He–$CO_2$ mixture to maximize the He fraction and thereby increase the gas collision rate, while maintaining a sufficient $CO_2$ pressure to provide the required nonlinearity. This configuration is tested at 20 and 40 kHz. At 20 kHz, the mixed-gas MPC restores the spectral coverage to a level comparable to that obtained in pure $CO_2$ at 10 kHz, as shown in Figure 3(a). The repetition rate is then increased to 40 kHz under mixed-gas conditions, where the spectral coverage remains comparable to that of the pure $CO_2$ MPC at 20 kHz. The output power stability at 40 kHz exhibits a root-mean-square (RMS) fluctuation of only 0.12%, confirming that the mixed-gas MPC provides stable high-repetition-rate signal generation.

Downloaded from https://www.cambridge.org/core. 18 Nov 2026 at 09:51:23, subject to the Cambridge Core terms of use.

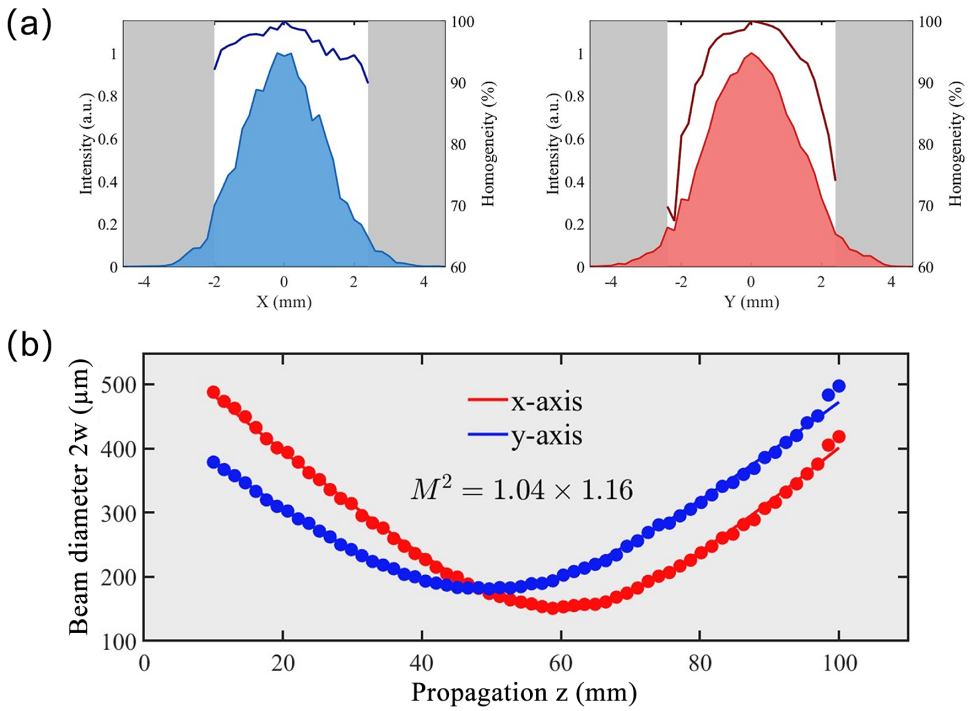



**Figure 4.** Signal-beam quality after the He–$CO_2$ MPC at 40 kHz. (a) Spatial–spectral homogeneity and (b) beam quality factor $M^2$.

Beam pointing provides a sensitive indicator of residual thermal perturbations. As shown in Figure 3(b), the pointing fluctuations at the MPC output are measured over 10 min. In pure $CO_2$, the RMS pointing fluctuation increases from $2.54 \times 1.92$ μrad at 1 kHz to $14.33 \times 19.73$ μrad at 20 kHz. With the He–$CO_2$ mixture, the 20 kHz pointing fluctuation is reduced to $10.51 \times 7.90$ μrad, whereas it increases to $20.61 \times 19.17$ μrad at 40 kHz. This degradation is attributed to residual thermally induced refractive-index fluctuations in the molecular gas, and additional thermal management generally improves the beam pointing stability of the MPC output at high repetition rates.

At 40 kHz, with 140 μJ input pulses and a gas mixture of 2 bar $CO_2$ and 2 bar He, the spatial–spectral homogeneity and beam quality of the Raman-shifted MPC output are characterized. The spatial–spectral homogeneity is quantified by the following:

$$V(x) = \frac{\left[\int I(x,\lambda)\, I_0(\lambda)\, \mathrm{d}\lambda\right]^2}{\int I(x,\lambda)^2 \mathrm{d}\lambda \int I_0(\lambda)^2 \mathrm{d}\lambda},$$

where $I(x,\lambda)$ is the local spectrum at transverse position $x$ and $I_0(\lambda)$ is the on-axis spectrum[37]. A 100-μm-core multimode fiber is scanned across the collimated beam in both the $x$ and $y$ directions with a 200 μm step size. As shown in Figure 4(a), the homogeneity factors are $V_x = 97\%$ and $V_y = 95\%$. The beam quality measurement in Figure 4(b) yields $M^2 = 1.04 \times 1.16$. The high spatial–spectral homogeneity and near-diffraction-limited beam quality are essential because efficient DFG requires good spatial overlap, stable phase matching and a clean signal wavefront.

### *3.3. Microjoule-level tunable 5.6–11 μm mid-infrared generation*

At a fixed input pulse energy of 140 μJ, tunable signal pulses in the 1.10–1.25 μm range are obtained by varying the gas pressure from 1.6 to 4 bar and filtering the Raman-shifted long-wavelength sidebands, as shown in Figure 5(a). The filtered-signal conversion efficiency is 17%–32% and decreases with increasing signal wavelength. The conversion efficiency is given by the product of the MPC transmission efficiency and the Raman frequency-shifting efficiency. This value is substantially higher than that typically achieved in white-light-seeded signal arms of OPA-based DFG systems. Further increasing the reflectivity of the MPC mirrors is expected to enhance the signal conversion efficiency in future work.

The filtered signal exhibits a broader spectral bandwidth than the 1025 nm pump. For example, at a signal center wavelength of 1170 nm, the filtered bandwidth is approximately 24 nm, corresponding to a Fourier-transform-limited (FTL) pulse duration of approximately 70 fs, whereas the measured autocorrelation gives a $\mathrm{sech}^2$-fitted pulse duration of approximately 97 fs, as shown in Figure 5(b). Although short signal pulses are beneficial for broadband DFG, they provide a limited temporal-overlap window in a millimeter-scale LGS crystal and can also increase the risk of

Downloaded from https://www.cambridge.org/core. 18 Nov 2026 at 09:51:23, subject to the Cambridge Core terms of use.

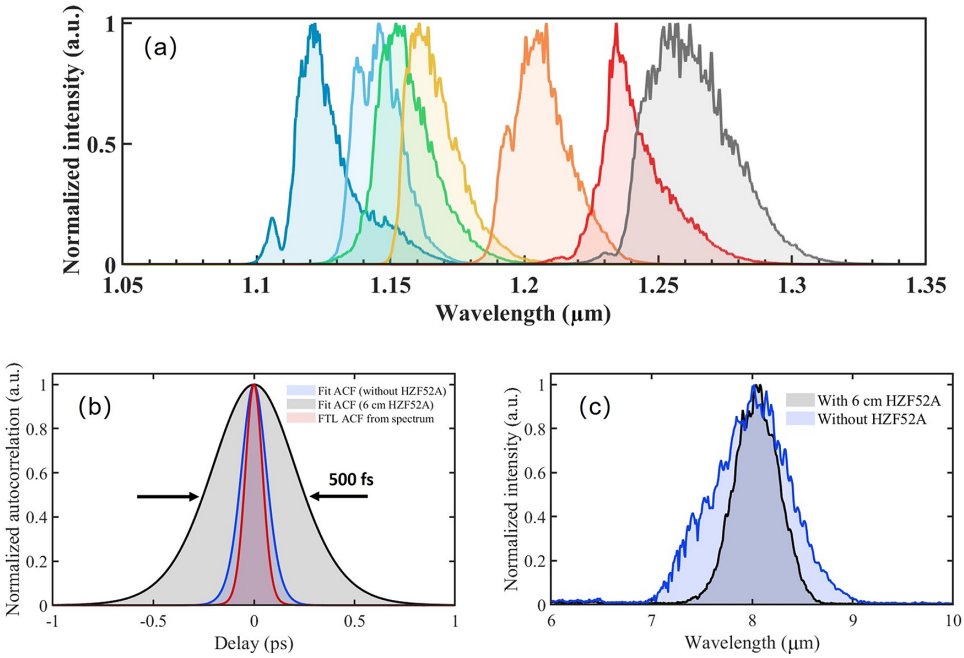



**Figure 5.** Tunable Raman-shifted signal generation and its influence on DFG. (a) Filtered-signal spectra obtained from the He–$CO_2$ MPC by varying the gas pressure. (b) Autocorrelation traces of the filtered 1170 nm signal before and after HZF52A stretching. (c) DFG spectra centered at 8 μm measured with and without HZF52A glass.

optical damage due to their high peak power. Therefore, the signal pulses are positively chirped using highly dispersive HZF52A glass. HZF52A provides a group-delay dispersion of 92–131 $fs^2$/mm over the 1.1–1.3 μm range[39]. After 6 cm of HZF52A, the autocorrelation broadens to approximately 500 fs, corresponding to a $sech^2$-fitted pulse duration of approximately 320 fs and reducing the signal peak power by approximately a factor of three.

Figure 5(c) compares DFG spectra centered at 8 μm with and without the HZF52A glass under a 2 W pump and a 0.4 W signal. Without chirping, the DFG output power is approximately 100 mW. With the chirped signal, the output power increases to approximately 108 mW despite the reduced peak power. This improvement indicates that temporal overlap over the 5.6 mm LGS crystal is more favorable for the chirped signal under the present energy-scaling conditions. The spectral bandwidth narrows from approximately 0.8 μm to approximately 0.5 μm because only the temporally overlapping spectral slice of the chirped signal contributes efficiently to DFG. Thus, near-FTL signals are preferable for broadband few-cycle mid-infrared generation, whereas chirped signals are advantageous here for improving the damage margin and energy scalability.

With a maximum signal energy of 20 μJ and a pump energy of 70 μJ, corresponding to a peak intensity of approximately 31 GW/$cm^2$ in the LGS crystal, tunable mid-infrared spectra covering 5.6–11 μm are obtained by adjusting the signal central wavelength and the LGS phase-matching angle, as shown in Figure 6(a).

Figures 6(b) and 6(c) show the mid-infrared output powers at 6, 7, 8, 9 and 10 μm as functions of pump power at a fixed signal energy of 20 μJ and signal power at a fixed pump energy of 70 μJ, respectively. The output power decreases toward a longer wavelength, primarily due to the photon-energy scaling governed by the Manley–Rowe relation. A more pronounced efficiency reduction is observed beyond 9 μm, which is likely caused by increased absorption in LGS in this spectral region. The signal-power dependence shows clear saturation as the signal energy approaches 20 μJ, suggesting that, under the current operating conditions, further idler scaling should rely mainly on increasing the pump energy while controlling the intensity in the crystal.

The maximum output power reaches 179 mW at 6 μm, corresponding to a pulse energy of 4.5 μJ, an energy conversion efficiency of 6.4% and a quantum efficiency of 37%. The energy conversion efficiency is calculated as the ratio of the generated mid-infrared power to the pump power incident on the LGS crystal. The spectral bandwidth is approximately 0.18 μm, corresponding to an FTL pulse duration of 208 fs. At 7 μm, the output power reaches 168 mW, corresponding to 4.2 μJ pulses, a conversion efficiency of 6% and a maximum quantum efficiency of 41%. The bandwidth is approximately 0.26 μm, corresponding to an FTL duration of 196 fs. The high efficiency is enabled by the large signal energy produced by the Raman-shifted MPC, together with its excellent beam quality and spatial–spectral homogeneity. For comparison, at a signal power of 50 mW, a level typical of many OPA-based signal arms, the 6 μm output power is only 52 mW. Raising the signal

Downloaded from https://www.cambridge.org/core. 18 Nov 2026 at 09:51:23, subject to the Cambridge Core terms of use.

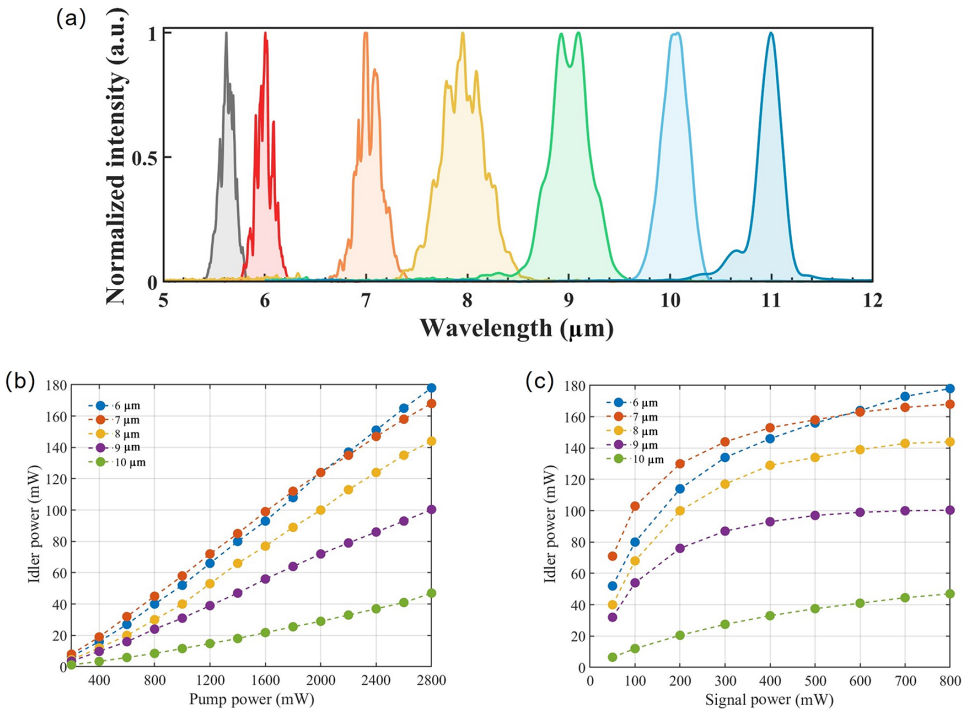



**Figure 6.** Tunable long-wave mid-infrared DFG output. (a) Representative spectra covering 5.6–11 μm. Output power at 6, 7, 8, 9 and 10 μm as a function of (b) pump power and (c) signal power.

power through the Raman-shifted MPC therefore produces an approximately threefold increase in mid-infrared output power under otherwise similar pump conditions.

We measured the short-term power and pointing stability of the 6 μm mid-infrared output over 10 min, as shown in Figure 7. The RMS power fluctuation is 0.85%, indicating low-intensity noise for the DFG output. The RMS pointing fluctuations are 11.99 and 9.72 μrad in the $x$ and $y$ directions, respectively. These values are lower than those of the signal-generating He–$CO_2$ MPC, which is reasonable since the DFG beam inherits pointing fluctuations from both interacting near-infrared beams. The pump-delay He-filled MPC, operating in a nearly linear regime, typically exhibits better pointing stability, with RMS pointing fluctuations of 10.58 and 6.89 μrad in the $x$ and $y$ directions, respectively.

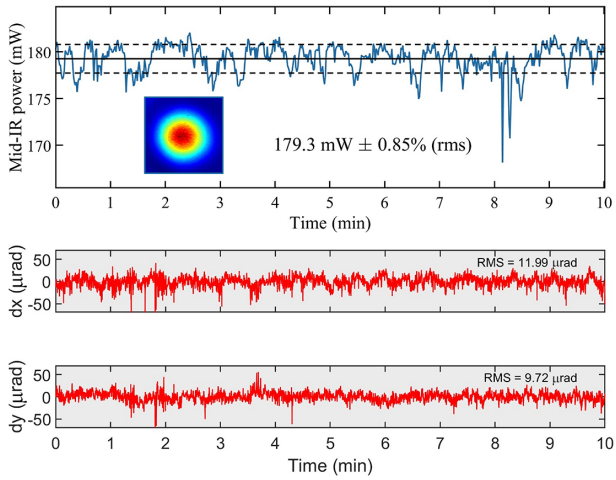



**Figure 7.** Power and beam pointing stability of the 6 μm mid-infrared output measured over 10 min.

## 4. Discussion

The results show that the Raman-shifted molecular-gas MPC directly addresses the signal-arm bottleneck in 1-μm-pumped long-wave mid-infrared DFG. The physical chain is straightforward: rotational Raman nonlinearity in $CO_2$ enhances red-shifted spectral broadening; filtering the long-wavelength sideband provides an energetic and high-quality 1.10–1.25 μm signal, and the large signal field then increases the DFG idler efficiency in LGS. Compared with an OPA-based signal chain, this scheme reduces the number of parametric stages while providing higher signal energy and excellent spatial quality. This is the primary reason why the system reaches 6.4% energy conversion efficiency and 41% quantum efficiency at 40 kHz.

The current output scaling is mainly limited by the pump intensity that can be safely applied to the LGS crystal. The signal-power dependence in Figure 6(c) already shows saturation near the maximum available signal energy, so increasing the pump energy is the most direct route to higher pulse energy and average power. Chirping both the pump and signal pulses, as well as increasing the beam diameter in a

Downloaded from https://www.cambridge.org/core. 18 Nov 2026 at 09:51:23, subject to the Cambridge Core terms of use.

larger-aperture LGS crystal, can reduce the peak intensity while enabling higher pulse energy. According to Ref. [21], by expanding the beam diameter to approximately 3 mm and chirping the pulses to the picosecond regime, the input pump energy can be scaled to the millijoule level, enabling a several-fold increase in the mid-infrared pulse energy. At a repetition rate of 40 kHz, this projected operating point would enable both tens-of-microjoule pulse energy and watt-level average power in the long-wave mid-infrared region. Further improvements may be achieved by increasing the signal energy at higher pump levels, employing type-II phase matching in LGS to exploit a larger effective nonlinear coefficient, and using a thinner crystal to mitigate self-focusing and walk-off effects, thereby facilitating scaling toward higher average power pulse energy.

Repetition-rate scaling is the second route to higher average power. The present results identify thermal effects in the molecular gas as the main limitation. The He–$CO_2$ mixture partly restores the Raman-shifted spectral coverage and enables stable operation at 40 kHz, but residual thermally induced index fluctuations still contribute to pointing noise. Future optimization should therefore focus on gases and gas-handling schemes that maintain a strong Raman response while improving heat removal. Possible strategies include optimizing the He/$CO_2$ mixing ratio, increasing gas flow or refreshing it and applying differential pumping concepts that have been demonstrated in hollow-core-fiber systems[36,37]. Given the intrinsically higher tolerance of MPC geometries to mode distortion compared with waveguides, these measures may enable further repetition-rate scaling without sacrificing transmission efficiency.

Finally, the trade-off between energy scalability and mid-infrared bandwidth should be considered. Chirping the signal improves temporal overlap and lowers peak intensity in the present long-crystal, high-energy DFG configuration, but it also narrows the idler bandwidth. Previous studies have shown that broadband few-cycle mid-infrared generation in DFG is governed by the nonlinear-crystal phase-matching bandwidth and the signal spectrum[40,41]. For few-cycle long-wave mid-infrared generation, near-FTL broadband Raman-shifted signals combined with thinner LGS crystals may be more suitable. The demonstrated compressibility of Raman-broadened spectra in molecular-gas systems[32,42] suggests that Raman-shifted MPCs could also serve as front ends for broadband, CEP-stable few-cycle long-wave mid-infrared generation.

## 5. Conclusion

We have demonstrated an efficient Raman-shifted MPC-driven DFG scheme for tunable 5.6–11 μm ultrafast generation. A He–$CO_2$ molecular-gas MPC produces a tunable 1.10–1.25 μm signal with 17%–32% filtered conversion efficiency at repetition rates up to 40 kHz. After DFG in LGS, the system delivers 4.5 μJ pulses at 6 μm with 179 mW average power and 6.4% energy conversion efficiency, and 4.2 μJ pulses at 7 μm with 168 mW average power and 41% quantum efficiency. The 6 μm output exhibits an RMS power fluctuation of 0.85% and beam pointing fluctuations of $11.99 \times 9.72$ μrad over 10 min. The high efficiency results from replacing the conventional OPA-based signal chain with an efficient Raman-shifted molecular-gas MPC that provides high signal energy, good spatial–spectral homogeneity and near-diffraction-limited beam quality. This approach provides a scalable path toward high-repetition-rate, high-energy and potentially few-cycle long-wave mid-infrared sources for spectroscopy, strong-field physics and resonant laser–matter interaction.

## Acknowledgements

This work was supported by the National Natural Science Foundation of China (NSFC) (Grant No. 62427901).

## References

1. J. G. Crowder, S. D. Smith, A. Vass, and J. Keddie, *Infrared Methods for Gas Detection* (Springer London, London, 2006), pp. 595–613.
2. K. C. Cossel, E. M. Waxman, I. A. Finneran, G. A. Blake, J. Ye, and N. R. Newbury, J. Opt. Soc. Am. B **34**, 104 (2017).
3. I. K. Ilev and R. W. Waynant, *Mid-Infrared Biomedical Applications* (Springer London, London, 2006), pp. 615–634.
4. M. J. Walsh, R. K. Reddy, and R. Bhargava, IEEE J. Sel. Top. Quantum Electron. **18**, 1502 (2012).
5. M. Pilling and P. Gardner, Chem. Soc. Rev. **45**, 1935 (2016).
6. R. Zgadzaj, J. Welch, Y. Cao, L. D. Amorim, A. Cheng, A. Gaikwad, P. Iapozzutto, P. Kumar, I. Petrushina, R. Samulyak, N. Vafaei-Najafabadi, C. Joshi, C. Zhang, M. Babzien, M. Fedurin, R. Kupfer, K. Kusche, M. A. Palmer, I. V. Pogorelsky, M. N. Polyanskiy, C. Swinson, and M. C. Downer, Nat. Commun. **15**, 4037 (2024).
7. G. Vampa, T. J. Hammond, N. Thiré, B. E. Schmidt, F. Légaré, C. R. McDonald, T. Brabec, and P. B. Corkum, Nature **522**, 462 (2015).
8. X. Yang, D. Zhang, W. Wang, K. Tian, L. He, J. Guo, B. Hu, T. Pu, W. Li, S. Sun, C. Ding, H. Wu, W. Li, Y. Peng, J. Li, Y. Leng, and H. Liang, Laser Photonics Rev. **19**, 2401856 (2025).
9. Z. Fu, X. Yang, K. Tian, J. Guo, M. Xiang, D. Zhang, L. He, A. Deng, Y. Wang, X. Peng, H. Wu, B. Hu, W. Chang, Q. J. Wang, S. L. G. Anderson, and H. Liang, Laser Photonics Rev. **20**, e00874 (2026).
10. Z. Heiner, V. Petrov, and M. Mero, Opt. Lett. **45**, 5692 (2020).
11. L. von Grafenstein, M. Bock, D. Ueberschaer, K. Zawilski, P. Schunemann, U. Griebner, and T. Elsaesser, Opt. Lett. **42**, 3796 (2017).
12. J. Sang, J. Gao, H. Li, Y. Fang, L. Song, Y. Tian, and R. Li, Opt. Laser Technol. **184**, 112573 (2025).
13. X. Gu, Y. Ding, Z. Hu, P. Yuan, D. Zhang, J. Wang, G. Xie, J. Ma, and L. Qian, Laser Photonics Rev. **19**, 2400507 (2025).
14. H. Li, L. Song, Y. Tian, and R. Li, Laser Photonics Rev. **20**, e02847 (2026).
15. L. He, W. Wang, K. Tian, M. Xiang, Z. Wan, B. Hu, Y. Li, H. Wu, Z.-Y. Chen, F. Yang, and H. Liang, Ultrafast Science **3**, 0022 (2023).

Downloaded from https://www.cambridge.org/core. 18 Nov 2026 at 09:51:23, subject to the Cambridge Core terms of use.

16. I. Pupeza, D. Sánchez, J. Zhang, N. Lilienfein, M. Seidel, N. Karpowicz, T. Paasch-Colberg, I. Znakovskaya, M. Pescher, W. Schweinberger, V. Pervak, E. Fill, O. Pronin, Z. Wei, F. Krausz, A. Apolonski, and J. Biegert, Nat. Photonics **9**, 721 (2015).
17. B.-H. Chen, T. Nagy, and P. Baum, Opt. Lett. **43**, 1742 (2018).
18. Q. Cao, F. X. Kärtner, and G. Chang, Opt. Express **28**, 1369 (2020).
19. B. Liu, H. Bromberger, A. Cartella, T. Gebert, M. Först, and A. Cavalleri, Opt. Lett. **42**, 129 (2017).
20. K. Kato, K. Miyata, L. Isaenko, S. Lobanov, V. Vedenyapin, and V. Petrov, Opt. Lett. **42**, 4363 (2017).
21. S. Qu, H. Liang, K. Liu, X. Zou, W. Li, Q. J. Wang, and Y. Zhang, Opt. Lett. **44**, 2422 (2019).
22. M. Seidel, X. Xiao, S. A. Hussain, G. Arisholm, A. Hartung, K. T. Zawilski, P. G. Schunemann, F. Habel, M. Trubetskov, V. Pervak, O. Pronin, and F. Krausz, Sci. Adv. **4**, eaaq1526 (2018).
23. C. Grebing, M. Müller, J. Buldt, H. Stark, and J. Limpert, Opt. Lett. **45**, 6250 (2020).
24. M. Kaumanns, D. Kormin, T. Nubbemeyer, V. Pervak, and S. Karsch, Opt. Lett. **46**, 929 (2021).
25. J. Su, Y. Luo, Z. Li, G. Chang, and W. Liu, Appl. Phys. B **131**, 123 (2025).
26. Q. Bournet, F. Guichard, M. Natile, Y. Zaouter, M. Joffre, A. Bonvalet, I. Pupeza, C. Hofer, F. Druon, M. Hanna, and P. Georges, Opt. Lett. **47**, 261 (2022).
27. R. Safaei, G. Fan, O. Kwon, K. Légaré, P. Lassonde, B. E. Schmidt, H. Ibrahim, and F. Légaré, Nat. Photonics **14**, 733 (2020).
28. C. Feng and J. Bromage, Opt. Express **34**, 6073 (2026).
29. L. Shen, J. Jiang, J. Song, Y. Peng, Y. Liu, G. Gao, J. Zhu, T. Xu, X. Lu, and Y. Leng, Opt. Lett. **50**, 2398 (2025).
30. A. B. Wahid, V. Hariton, K. Fritsch, and O. Pronin, in *2021 Conference on Lasers and Electro-Optics Europe & European Quantum Electronics Conference (CLEO/Europe-EQEC)* (IEEE, 2021).
31. M. Kadiwala, N. Kovalenko, K. Fritsch, S. Goncharov, and O. Pronin, EPJ Web Conf. **267**, 02032 (2022).
32. J. E. Beetar, M. Nrisimhamurty, T.-C. Truong, G. C. Nagar, Y. Liu, J. Nesper, O. Suarez, F. Rivas, Y. Wu, B. Shim, and M. Chini, Sci. Adv. **6**, eabb5375 (2020).
33. I. Kinyaevskiy, A. Koribut, Y. Grudtsyn, and M. Ionin, Opt. Lett. **50**, 2267 (2025)
34. C. Bree, A. Demircan, and G. Steinmeyer, IEEE J. Quantum Electron. **46**, 433 (2010).
35. S. Goncharov, K. Fritsch, and O. Pronin, Opt. Lett. **48**, 147 (2023).
36. J. E. Beetar, M. Nrisimhamurty, T.-C. Truong, Y. Liu, and M. Chini, Opt. Lett. **46**, 2437 (2021).
37. L. Arias, A. Longa, G. Jargot, A. Pomerleau, P. Lassonde, G. Fan, R. Safaei, P. B. Corkum, F. Boschini, H. Ibrahim, and F. Légaré, Opt. Lett. **47**, 3612 (2022).
38. J. Weitenberg, A. Vernaleken, J. Schulte, A. Ozawa, T. Sartorius, V. Pervak, H.-D. Hoffmann, T. Udem, P. Russbüldt, and T. W. Hänsch, Opt. Express **25**, 20502 (2017).
39. M. N. Polyanskiy, Sci. Data **11**, 94 (2024).
40. K. Liu, H. Liang, L. Wang, S. Qu, T. Lang, H. Li, Q. J. Wang, and Y. Zhang, Opt. Lett. **44**, 1003 (2019).
41. B.-H. Chen, E. Wittmann, Y. Morimoto, P. Baum, and E. Riedle, Opt. Express **27**, 21306 (2019).
42. K. Légaré, R. Safaei, G. Barrette, L. Arias, P. Lassonde, H. Ibrahim, B. Vodungbo, E. Jal, J. Lüning, N. Jaouen, Z. Tao, A. Baltuška, F. Légaré, and G. Fan, Adv. Photonics Res. **2**, 2100113 (2021).

Downloaded from https://www.cambridge.org/core. 18 Nov 2026 at 09:51:23, subject to the Cambridge Core terms of use.